

## Benchmark computations of diffuse interface models for two-dimensional bubble dynamics

S. Aland<sup>\*,†</sup> and A. Voigt

*Institut für Wissenschaftliches Rechnen, Dresden, Germany*

### SUMMARY

Diffuse interface models for incompressible two-phase flow with large density ratios are tested on benchmark configurations for a two-dimensional bubble rising in liquid columns. The benchmark quantities circularity, center of mass, and mean rise velocity are compared with reference solutions from Hysing *et al.* Copyright © 2011 John Wiley & Sons, Ltd.

Received 7 January 2011; Revised 20 April 2011; Accepted 24 April 2011

KEY WORDS: two-phase flow; bubble dynamics; benchmark; diffuse interface approximation

### 1. INTRODUCTION

In [1], a numerical benchmark configuration has been proposed for two-dimensional bubble dynamics. Two benchmark test cases have been considered, both concern the evolution of a single bubble rising in a liquid column while undergoing shape deformations. The first with a small density and viscosity ratio, for which the bubble undergoes only moderate shape deformations, and the second with a bubble with a very low density compared with the surrounding fluid, which leads to large deformations and topological changes. Different numerical approaches have been quantitatively compared, among them are Eulerian level set finite element methods as well as an arbitrary Lagrangian–Eulerian moving grid approach. Diffuse interface approximations for two-phase flow problems have not been considered so far. We will test finite element discretizations of different diffuse interface models for two-phase flow problems on both benchmark test cases. Diffuse interface approximations have been successfully used to describe two-phase flow problems with constant density in both phases for various applications. The model dates back to Hohenberg and Halperin [2] and is called ‘Model H’. Gurtin *et al.* [3] showed thermodynamic consistency of this model. To treat problems with small density ratios, a common practice is to use a Boussinesq approximation where an external gravitational force is added to model the effect of a density difference. The achieved model remains thermodynamically consistent. The approach however is not valid for large density ratios. Lowengrub and Trusniowski [4] derived a thermodynamically consistent extension to the ‘Model H’, which allows also for large differences in densities. However, the velocity field is no longer divergence free, and the coupling between the Navier–Stokes equation and the evolution equation of the phase field function becomes much stronger, which makes numerical computations harder. Alternative generalizations for different densities have been discussed by Boyer [5], Ding *et al.* [6], Shen and Yang [7], and most recently by Abels *et al.* [8]. In all approaches, the velocity remains divergence free; thermodynamic consistency however could only be shown for the models proposed in [7, 8].

<sup>\*</sup>Correspondence to: S. Aland, Institut für Wissenschaftliches Rechnen, TU Dresden, 01062, Dresden, Germany.

<sup>†</sup>E-mail: sebastian.aland@tu-dresden.de

The outline of the paper is as follows. Section 2 introduces the governing equations in the classical sharp interface setting. The diffuse interface approximations are considered in Section 3, and their numerical treatment is described in Section 4. The test cases and results are presented and compared in Section 5. Conclusions are drawn in Section 6.

## 2. MATHEMATICAL MODEL

We consider isothermal, incompressible flow of two immiscible fluids. In the classical approach, the interface between both fluids is usually considered as a free boundary that evolves in time. The movement of the interface is determined by a set of interfacial balance conditions. The governing equations read

$$\rho_i \left( \frac{\partial \mathbf{u}_i}{\partial t} + \mathbf{u}_i \cdot \nabla \mathbf{u}_i \right) = -\nabla p_i + \nabla \cdot (\nu_i \mathbf{D}(\mathbf{u}_i)) + \mathbf{F}_i, \quad \text{in } \Omega_i \quad (1)$$

$$\nabla \cdot \mathbf{u}_i = 0, \quad \text{in } \Omega_i \quad (2)$$

where  $\Omega_i \subset \mathcal{R}^2$ , for  $i = 1, 2$  denotes the domain, and  $\rho_i$ ,  $\mathbf{u}_i$ ,  $p_i$ ,  $\nu_i$ ,  $\mathbf{F}_i$  are the density, velocity, pressure, viscosity, and body force in domain  $\Omega_i$ , respectively. Across the interface  $\Sigma$  separating the domains, the following jump conditions hold:

$$[\mathbf{u}]_\Sigma = \mathbf{0}, \quad [-p\mathbf{I} + \nu \mathbf{D}(\mathbf{u})]_\Sigma \cdot \mathbf{n} = -\sigma \kappa \mathbf{n}, \quad (3)$$

where  $[f]_\Sigma = f_1 - f_2$  denotes the jump in  $f$  across  $\Sigma$ ,  $\mathbf{I}$  is the identity tensor,  $\mathbf{D}(\mathbf{u}) = (\nabla \mathbf{u} + (\nabla \mathbf{u})^T)$ ,  $\mathbf{n}$  is the normal vector to  $\Sigma$  pointing into  $\Omega_2$ ,  $\sigma$  is the surface tension,  $\kappa$  is the mean curvature of the interface (positive for a sphere), and  $\nabla_\Sigma = (\mathbf{I} - \mathbf{nn}) \nabla$  is the surface gradient. Let  $\Omega = \Omega_1 \cup \Sigma \cup \Omega_2$ . It is assumed that fluid 1 occupies the domain  $\Omega_1$  and that it completely surrounds fluid 2 in  $\Omega_2$ . Therefore,  $\partial\Omega_2 \cap \partial\Omega = \emptyset$ . As boundary conditions, we take the no-slip condition  $\mathbf{u}_1 = \mathbf{0}$  at the top and bottom boundaries in a rectangular domain, as well as the free-slip condition  $\mathbf{u}_1 \cdot \mathbf{n} = \mathbf{t} \cdot \mathbf{D}(\mathbf{u}_1) \cdot \mathbf{n} = 0$ , with the tangent vector  $\mathbf{t}$ , on the vertical walls.

## 3. DIFFUSE INTERFACE APPROXIMATION

An alternative to direct approaches for solving such interface problems is the diffuse interface method, which was originally developed to model solid–liquid phase transitions (see e.g., [9–11]). The interface thereby is represented as a thin layer of finite thickness, and an auxiliary function, the so-called phase field function, is used to indicate the phases. The phase field function varies smoothly between distinct values in both phases, and the interface can be associated with an intermediate level set of the phase field function. Diffuse interface approaches for mixtures of two immiscible, incompressible fluids lead to the Navier–Stokes–Cahn–Hilliard equations and have been considered by several authors (see e.g., [12–15]). The model reads as follows:

$$\rho (\partial_t \mathbf{u} + (\mathbf{u} \cdot \nabla) \mathbf{u}) = -\nabla \tilde{p} + \nabla \cdot (\nu \mathbf{D}(\mathbf{u})) + \mathbf{F} + \mu \nabla c, \quad (4)$$

$$\nabla \cdot \mathbf{u} = 0, \quad (5)$$

$$\partial_t c + \mathbf{u} \cdot \nabla c = \nabla \cdot (M(c) \nabla \mu), \quad (6)$$

$$\mu = \tilde{\sigma} \epsilon^{-1} W'(c) - \tilde{\sigma} \epsilon \Delta c, \quad (7)$$

in the domain  $\Omega$ . Here  $\mathbf{u}$ ,  $\tilde{p}$ ,  $c$  and  $\mu$  are the velocity, pressure, phase field variable, and chemical potential, respectively. The relation between  $\tilde{p}$  and the physical pressure  $p$  is thereby given through  $\tilde{p} = p + \frac{\tilde{\sigma} \epsilon}{2} |\nabla c|^2 + \frac{\tilde{\sigma}}{\epsilon} W(c)$ . The function  $W(c)$  is a double well potential, here we use  $W = 1/4(c^2 - 1)^2$  such that  $c \approx 1$  in  $\Omega_1$  and  $c \approx -1$  in  $\Omega_2$ . The function  $M(c)$  is a mobility, here we use  $M(c) = \gamma(c^2 - 1)^2$ , where  $\gamma$  is a constant mobility coefficient.  $\epsilon$  defines a length scale over which the interface is smeared out. Furthermore,  $\rho$ ,  $\nu$ , and  $\mathbf{F}$  are again the density, viscosity,

and body force, respectively. The parameter  $\tilde{\sigma}$  is a scaled surface tension, which is related to the physical surface tension by  $\tilde{\sigma} = \sigma \frac{3}{2\sqrt{2}}$ .

The diffuse interface model converges to Equations (4)–(7) with  $\rho_1 = \rho_2 = \rho$  and  $\nu_1 = \nu_2 = \nu$  if the width of the interfacial layer  $\epsilon$  tends to zero. This can at least be shown formally using matched asymptotic analysis.

The case of variable density and viscosity is more complicated. The model used in [6, 7] uses Equations (4)–(7) but with variable density and viscosity given by  $\rho(c) = \rho_1(c+1)/2 + \rho_2(c-1)/2$  and  $\nu(c) = \nu_1(c+1)/2 + \nu_2(c-1)/2$ , respectively. The model reads as follows:

Model 1

$$\rho(c) (\partial_t \mathbf{u} + (\mathbf{u} \cdot \nabla) \mathbf{u}) = -\nabla \tilde{p} + \nabla \cdot (\nu(c) \mathbf{D}(\mathbf{u})) + \mathbf{F} + \mu \nabla c, \quad (8)$$

$$\nabla \cdot \mathbf{u} = 0, \quad (9)$$

$$\partial_t c + \mathbf{u} \cdot \nabla c = \nabla \cdot (M(c) \nabla \mu), \quad (10)$$

$$\mu = \tilde{\sigma} \epsilon^{-1} W'(c) - \tilde{\sigma} \epsilon \Delta c. \quad (11)$$

Following Guermond and Quartapelle [16], an energy estimate of the model could be shown by introducing the new variable  $r = \sqrt{\rho}$ , see [7]. Boyer [5] followed a different approach. The starting point for the derivation are the equations of linear momentum of each fluid. The model reads as follows:

Model 2

$$\rho(c) (\partial_t \mathbf{u} + (\mathbf{u} \cdot \nabla) \mathbf{u}) = -\nabla \tilde{p} + \nabla \cdot (\nu(c) \mathbf{D}(\mathbf{u})) + \mathbf{F} + \mu \nabla c \quad (12)$$

$$+ (\rho_2 - \rho_1) \frac{1 - c^2}{4} \nabla \frac{\mu}{\rho(c)}, \quad (13)$$

$$\nabla \cdot \mathbf{u} = 0, \quad (14)$$

$$\partial_t c + \mathbf{u} \cdot \nabla c = \nabla \cdot \left( \frac{M(c)}{\rho(c)} \nabla \frac{\mu}{\rho(c)} \right), \quad (15)$$

$$\mu = \tilde{\sigma} \epsilon^{-1} W'(c) - \tilde{\sigma} \epsilon \Delta c, \quad (16)$$

Neither global nor local energy inequalities seem to be known for this model. Abels *et al.* [8] considered the following thermodynamically consistent model:

Model 3

$$\partial_t (\rho(c) \mathbf{u}) + \nabla \cdot (\rho(c) \mathbf{u} \otimes \mathbf{u}) = -\nabla \tilde{p} + \nabla \cdot (\nu(c) \mathbf{D}(\mathbf{u})) + \mathbf{F} + \mu \nabla c \quad (17)$$

$$- \nabla \cdot \left( \mathbf{u} \otimes \frac{\rho_1 - \rho_2}{2} M(c) \nabla \mu \right), \quad (18)$$

$$\nabla \cdot \mathbf{u} = 0, \quad (19)$$

$$\partial_t c + \mathbf{u} \cdot \nabla c = \nabla \cdot (M(c) \nabla \mu), \quad (20)$$

$$\mu = \tilde{\sigma} \epsilon^{-1} W'(c) - \tilde{\sigma} \epsilon \Delta c, \quad (21)$$

for which also convergence for  $\epsilon \rightarrow 0$  is shown using a formal matched asymptotic analysis.

#### 4. FINITE ELEMENT DISCRETIZATION

For the numerical solution of the three models, we adapt existing algorithms for the Navier–Stokes–Cahn–Hilliard equation (e.g., [17, 18]). Let  $T_h$  be a triangulation of the domain  $\Omega$ , and let  $J_\tau = \{t_m\}_{m=0}^M$  be a quasi-uniform partition of  $[0, T]$  of mesh size  $\tau := \frac{T}{M}$ . Of course, adaptive time steps may also be used. We define the discrete time derivative  $d_t v^m := (v^m - v^{m-1})/\tau$ , where the upper index denotes the time step number. Furthermore, for a nonnegative integer  $r$ , let

$P_r(K)$  denote the space of polynomials of degree less than or equal to  $r$  on a triangle or tetrahedron  $K \in T_h$ . We introduce the finite element spaces

$$M_h = \{q \in L_0^2(\Omega) | q|_K \in P_{r_q}(K)\}, \quad (22)$$

$$V_h = \{v \in C^0(\bar{\Omega}) \cap H_0^1(\Omega) | v|_K \in P_{r_v}(K)\}, \quad (23)$$

$$Y_h = \{\psi \in C^0(\bar{\Omega}) | \psi|_K \in P_{r_\psi}(K)\} \quad (24)$$

and denote by  $\mathbf{V}_h = (V_h)^d$  the space of vector test functions in dimension  $d$ .

The Cahn–Hilliard and Navier–Stokes systems are solved separately in an operator splitting manner. For both systems, we use an implicit Euler time stepping algorithm. Higher-order algorithms for the individual systems are applicable as well (see e.g., [19]).

#### 4.1. Cahn–Hilliard system

At every time step, we first solve the Cahn–Hilliard equations and then solve the Navier–Stokes system. The finite element approximation of the convective Cahn–Hilliard equation reads as follows: find  $(c^m, \mu^m) \in Y_h \times Y_h$  such that for all  $(\psi, \xi) \in Y_h \times Y_h$

Model 1

$$(d_t c^m, \psi) + (\mathbf{u}^{m-1} \cdot \nabla c^m, \psi) + (M(c^{m-1}) \nabla \mu^m, \nabla \psi) = 0, \quad (25)$$

$$(\mu^m, \xi) - \tilde{\sigma} \epsilon (\nabla c^m, \nabla \xi) - \tilde{\sigma} \epsilon^{-1} (W'(c^m), \xi) = 0, \quad (26)$$

Model 2

$$(d_t c^m, \psi) + (\mathbf{u}^{m-1} \cdot \nabla c^m, \psi) + \left( \frac{M(c^{m-1})}{\rho^{m-1}} \nabla \mu^m, \nabla \psi \right) = 0, \quad (27)$$

$$(\rho^{m-1} \mu^m, \xi) - \tilde{\sigma} \epsilon (\nabla c^m, \nabla \xi) - \tilde{\sigma} \epsilon^{-1} (W'(c^m), \xi) = 0. \quad (28)$$

Model 3

$$(d_t c^m, \psi) + (\mathbf{u}^{m-1} \cdot \nabla c^m, \psi) + (M(c^{m-1}) \nabla \mu^m, \nabla \psi) = 0, \quad (29)$$

$$(\mu^m, \xi) - \tilde{\sigma} \epsilon (\nabla c^m, \nabla \xi) - \tilde{\sigma} \epsilon^{-1} (W'(c^m), \xi) = 0, \quad (30)$$

where  $(f, g)$  denotes the  $L^2(\Omega)$  inner product. We linearize the derivative of the double well potential  $W'(c^m)$  by a Taylor expansion of order one:

$$W'(c^m) \approx (c^{m-1})^3 - c^{m-1} + (3(c^{m-1})^2 - 1)(c^m - c^{m-1})$$

to obtain a linear system but keeping the non-linearity (semi)-implicit.

#### 4.2. Navier–Stokes system

After the Cahn–Hilliard system has been solved, we can define the variable density and viscosity by  $\rho^m = \rho_1(c^m + 1)/2 + \rho_2(c^m - 1)/2$  and  $\nu^m = \nu_1(c^m + 1)/2 + \nu_2(c^m - 1)/2$ , respectively. Because gravity is the only body force, we set  $\mathbf{F} = \rho \mathbf{g}$ , where  $\mathbf{g}$  denotes the gravitational vector field. Now, the finite element approximation for the Navier–Stokes equations is as follows: find  $(\mathbf{u}^m, p^m) \in \mathbf{V}_h \times M_h$  such that for all  $(\mathbf{v}, q) \in \mathbf{V}_h \times M_h$

Model 1

$$(\rho^m d_t \mathbf{u}^m, \mathbf{v}) + (\nu^m \mathbf{D}(\mathbf{u}^m), \nabla \mathbf{v}) + (\rho^m (\mathbf{u}^{m-1} \cdot \nabla) \mathbf{u}^m, \mathbf{v}) - (p^m, \nabla \cdot \mathbf{v}) \\ = (\rho^m \mathbf{g} + \mu^m \nabla c^m, \mathbf{v}), \quad (31)$$

$$(\nabla \cdot \mathbf{u}^m, q) = 0, \quad (32)$$

Model 2

$$(\rho^m d_t \mathbf{u}^m, \mathbf{v}) + (v^m \mathbf{D}(\mathbf{u}^m), \nabla \mathbf{v}) + (\rho^m (\mathbf{u}^{m-1} \cdot \nabla) \mathbf{u}^m, \mathbf{v}) - (p^m, \nabla \cdot \mathbf{v})$$

$$= (\rho^m \mathbf{g} + \rho^m \mu^m \nabla c^m + (\rho_2 - \rho_1) \frac{1 - (c^m)^2}{4} \nabla \mu, \mathbf{v}) \quad (33)$$

$$(\nabla \cdot \mathbf{u}^m, q) = 0, \quad (34)$$

Model 3

$$(d_t(\rho \mathbf{u})^m, \mathbf{v}) + (v^m \mathbf{D}(\mathbf{u}^m), \nabla \mathbf{v}) - (\rho^m \mathbf{u}^{m-1} \otimes \mathbf{u}^m, \nabla \mathbf{v}) - (\rho^m \mathbf{g} + \mu^m \nabla c^m, \mathbf{v})$$

$$= (p^m, \nabla \cdot \mathbf{v}) + \left( \mathbf{u}^m \otimes \frac{\rho_1 - \rho_2}{2} M(c^m) \nabla \mu^m, \nabla \mathbf{v} \right) \quad (35)$$

$$(\nabla \cdot \mathbf{u}^m, q) = 0. \quad (36)$$

#### 4.3. Numerical treatment

The adaptive finite element toolbox AMDiS [20] is used for discretization. We use a standard Taylor–Hood element for the Navier–Stokes equation with polynomial degree two for  $\mathbf{u}$  and one for  $p$ . The elements discretizing the concentration  $c$  and chemical potential  $\mu$  were chosen with polynomial degree two, although one could take elements of any polynomial degree. We did this to obtain equal basis functions for  $\mathbf{u}$  and  $c$  and thus to simplify the quantitative evaluation of the results using the open-source data analysis software PARAVIEW ([www.paraview.org](http://www.paraview.org)). The linearized system was solved using the direct unsymmetric multifrontal method (UMFPACK, [21]).

#### 4.4. Adaptivity

Adaptive meshes are indispensable for providing a high spatial resolution along the fluid–fluid interface described implicitly by  $c$ . To compare our results appropriately, we used a fixed resolution along the interface to control the grid sizes. Although the domain away from the interface is refined with an equidistant mesh of grid size  $h$ , we used a finer grid at the interface with grid size  $h_{\text{int}} = 1/8h$ , in all our simulations. The obtained meshes are similar to meshes generated using an  $L^2$ -like error indicator based on a jump residual (e.g., [20, 22]). Note that rigorous error estimates in  $h$  and  $\epsilon$  only exist for simpler problems like the Allen–Cahn equation (see [23]).

### 5. DEFINITION OF THE TEST AND RESULTS

#### 5.1. Test setup

The test setup is extensively described in [1]. The domain  $\Omega = [0, 1] \times [0, 2]$  is filled with fluid 1 ( $c \approx 1$ ) except for a circular bubble, which consists of fluid 2 ( $c \approx -1$ ). The initial bubble has a radius of 0.25 with its center at (0.5, 0.5). The parameters of the outer fluid are  $\rho_1 = 1000$ ,  $\mu_1 = 10$ . In the inner fluid,  $\rho_2 = 100$ ,  $\mu_2 = 1$  for test case 1 and  $\rho_2 = 1$  and  $\mu_2 = 0.1$  for test case 2. The gravitational force is given by  $\mathbf{g} = (0, 0.98)$ . The surface tension is  $\sigma = 24.5$  for test case 1 and  $\sigma = 1.96$  for test case 2.

Because the density of the bubble is smaller than the density of the surrounding fluid ( $\rho_2 < \rho_1$ ), the bubble rises. The evolution of the bubble is tracked for three time units during which the defined benchmark quantities are measured.

#### 5.2. Benchmark quantities and error quantification

For a rigorous estimation of the accuracy of the simulation, we used the same quantities as in [1]. The measured quantities are the following:

- center of mass

$$y_c = \frac{\int_{c < 0} y \, dx}{\int_{c < 0} 1 \, dx}$$

with  $y$  as the vertical coordinate  $(x, y) := \mathbf{x}$ ,

- circularity

$$c = \frac{\text{perimeter of area-equivalent circle}}{\text{perimeter of bubble}} = \frac{2\sqrt{\int_{c<0} \pi dx}}{P_b}$$

with the perimeter  $P_b$ , which is obtained by integration over a ‘contour’ filter in PARAVIEW.

- rise velocity

$$V_c = \frac{\int_{c<0} v dx}{\int_{c<0} 1 dx}$$

where  $v$  is the second (vertical) component of the velocity  $\mathbf{u}$ .

All defined quantities are time dependent. A relative error can be defined to measure their temporal evolution. We use the following error norms:

$$\|e\|_1 = \frac{\sum_{t=1}^{\text{NTS}} |q_{t,\text{ref}} - q_t|}{\sum_{t=1}^{\text{NTS}} |q_{t,\text{ref}}|}, \quad \|e\|_2 = \left( \frac{\sum_{t=1}^{\text{NTS}} |q_{t,\text{ref}} - q_t|^2}{\sum_{t=1}^{\text{NTS}} |q_{t,\text{ref}}|^2} \right)^{1/2}, \quad \|e\|_\infty = \frac{\max_t |q_{t,\text{ref}} - q_t|}{\max_t |q_{t,\text{ref}}|}$$

where  $q_t$  is the temporal evolution of quantity  $q$ . We take the data of group 3 from [1] on the finest grid as reference solution  $q_{t,\text{ref}}$ . Spline interpolation is used to match the time steps of the reference solution with our solution. Using the so defined errors, a rate of convergence (ROC) can be computed.

The numerical parameters used are shown in Table I. The mobility coefficient  $\gamma$  is an additional numerical parameter, which is not present in the sharp interface model. The value is chosen as small as possible according to the numerical performance. Because the coupling between Navier–Stokes and Cahn–Hilliard equation is carried out explicitly, the Courant–Friedrichs–Lewy condition  $\tau \lesssim h^{\frac{3}{2}}$  needs to be satisfied. However, we assume that the time step size here is sufficiently small that  $\tau$  can be refined proportional to  $h$ . Furthermore,  $\epsilon$  is chosen proportional to  $h$ , which keeps the number of elements along the interface fixed. Here, we have around three elements along the interface. As we use quadratic basis functions, this resolution is assumed to be sufficient because it is common to use 4–6 DOF along the interface.

### 5.3. Results for test case 1

The bubble, being initially circular, first stretches horizontally and develops a dimple at the bottom before it reaches a stable ellipsoidal shape. As in [1], we tabulate the total number of DOF, the total number of time steps, and the overall computing time in seconds (CPU) (see Table II). Because the implementation of the three models only differs in some terms, the measured CPU times are almost equal for all models.

Table I. Used numerical parameters for all computations: grid resolution  $h_{\text{int}}$ , diffuse interface width  $\epsilon$ , and time step size  $\tau$ . The mobility coefficient  $\gamma_{1,3}$  used for models 1 and 3 is different to  $\gamma_2$  used for model 2 because of the different definitions of the Cahn–Hilliard diffusion.

$h_{\text{int}}$	$\epsilon$	$\tau$	$\gamma_{1,3}$	$\gamma_2$
1/16	0.040	0.008	0.000040	40.0
1/32	0.020	0.004	0.000020	20.0
1/64	0.010	0.002	0.000010	10.0
1/128	0.005	0.001	0.000005	5.0

Table II. Simulation statistics and timings for model 1. The total number of degrees of freedom (NDOF), the total number of time steps (NTS), and the overall computing time in seconds (CPU). The values for models 2 and 3 differ only slightly.

$\epsilon$	NDOF <sup>1</sup>	NTS <sup>1</sup>	CPU <sup>1</sup>
0.040	2,900	375	140
0.020	6,400	750	600
0.010	14,800	1,500	3,240
0.005	39,800	3,000	18,240

Figure 1 shows the bubble shapes at the final time ( $t = 3$ ). The bubble shapes differ clearly for different values of  $\epsilon$  but seem to converge so that there is no obvious difference for the finest values  $\epsilon = 0.01$  and  $\epsilon = 0.005$ . The bubble shapes for model 2 is not similar to models 1 and 3 but seem to converge to the same shape as the other models do. No significant differences can be seen between the models 1 and 3.

It is clearly not sufficient to only look at the bubble shapes, therefore we use the previously defined benchmark quantities. Tables III–V show the quantitative comparison with the benchmark values for all three models. The line ‘ref’ gives a reference value from group 3 in [1]. One can see that each quantity approaches the reference value as  $\epsilon$  decreases.

Furthermore, we plot the circularity, center of mass, and rise velocity over time for all models (Figures 2–4). To increase the readability, we omit the coarsest grid results ( $\epsilon = 0.04$ ) here.

All the quantities seem to converge for each model. The plots for models 1 and 3 are indistinguishable, whereas model 2 reveals slightly different time evolutions of all quantities.

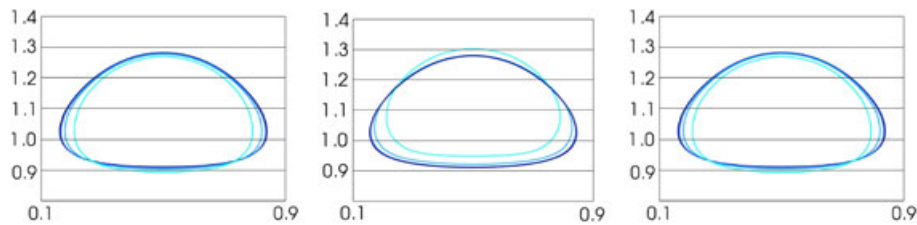


Figure 1. Bubble shapes at time  $t = 3$  for  $\epsilon = 0.04$  (light blue),  $\epsilon = 0.02$  (blue),  $\epsilon = 0.01$  (dark blue),  $\epsilon = 0.005$  (black) for models 1–3 (from left to right).

Table III. Model 1: Minimum circularity and maximum rise velocity, with corresponding incidence times and final position of the center of mass for test case 1.

$\epsilon$	$c_{\min}$	$t _{c=c_{\min}}$	$V_{c,\max}$	$t _{V_c=V_{c,\max}}$	$y_c(t=3)$
0.040	0.9322	1.936	0.2359	1.016	1.0692
0.020	0.9154	2.040	0.2380	1.040	1.0739
0.010	0.9062	1.996	0.2394	0.954	1.0768
0.005	0.9041	1.924	0.2402	0.929	1.0786
ref	0.9013	1.900	0.2417	0.924	1.0799

Table IV. Model 2: Minimum circularity and maximum rise velocity, with corresponding incidence times and final position of the center of mass for test case 1.

$\epsilon$	$c_{\min}$	$t _{c=c_{\min}}$	$V_{c,\max}$	$t _{V_c=V_{c,\max}}$	$y_c(t=3)$
0.040	0.9111	1.800	0.2530	0.960	1.1101
0.020	0.8924	1.792	0.2464	0.876	1.0862
0.010	0.8910	1.830	0.2439	0.904	1.0785
0.005	0.8946	1.843	0.2434	0.914	1.0779
ref	0.9013	1.900	0.2417	0.924	1.0799



Table V. Model 3: Minimum circularity and maximum rise velocity, with corresponding incidence times and final position of the center of mass for test case 1.

$\epsilon$	$c_{\min}$	$t _{c=c_{\min}}$	$V_{c,\max}$	$t _{V_c=V_{c,\max}}$	$y_c(t=3)$
0.040	0.9334	1.9440	0.2350	1.0160	1.0682
0.020	0.9159	2.0040	0.2375	1.0400	1.0733
0.010	0.9066	1.9910	0.2393	0.9530	1.0767
0.005	0.9045	1.9460	0.2401	0.9460	1.0785
ref	0.9013	1.9000	0.2417	0.9239	1.0817

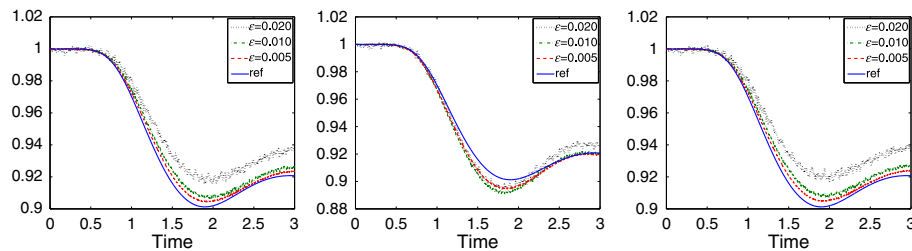


Figure 2. Circularity over time for test case 1 and models 1–3 (from left to right).

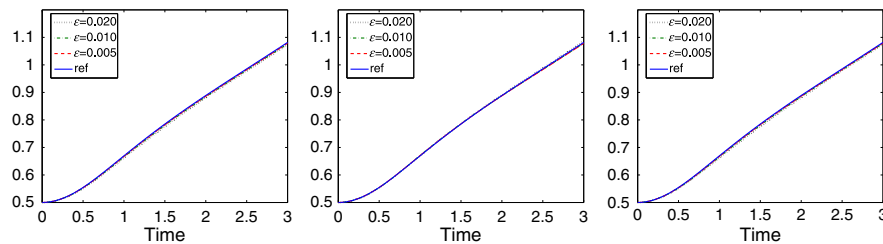


Figure 3. Center of mass over time for test case 1 and models 1–3 (from left to right).

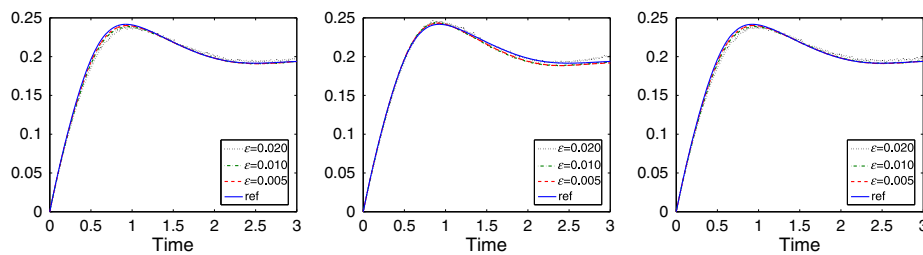


Figure 4. Rise velocity over time for test case 1 and models 1–3 (from left to right).

The relative error norms for the circularity, center of mass, and rise velocity are shown in Tables VI–VIII together with the estimated relative order of convergence (ROC). To calculate the ROC, we use the reference solution from [1]. The ROC is in all error norms around one for the models 1 and 3. For model 2, we obtain negative orders of convergence at some points. This indicates that this model does not (or not yet) converge to the reference solution. However, the relative errors are comparable with those of the models 1 and 3.

Note that in [1], the convergence has been calculated assuming the solution on the finest grid as exact solution. Hence, to be fair with the diffuse interface models, we also do this in the following. For each model, we assume its finest grid solution to be the exact solution and show errors and orders of convergence in Table IX. We only display the  $\|\cdot\|_1$  norm, but the results are very similar in the other two norms. The ROC is in all error norms between 1 and 2, for model 2 even above 2.

Next, we compare the solutions of the three different models. We plot the minimum circularity, maximum rise velocity, and final center of mass for all models versus the reference solution from



Table VI. Model 1: Relative error norms and convergence orders for test case 1.

$\epsilon$	$\ e\ _1$	ROC <sub>1</sub>	$\ e\ _2$	ROC <sub>2</sub>	$\ e\ _\infty$	ROC <sub><math>\infty</math></sub>
Center of mass						
0.040	0.0193		0.0205		0.0236	
0.020	0.0086	1.1619	0.0091	1.1738	0.0094	1.3280
0.010	0.0045	0.9483	0.0047	0.9512	0.0046	1.0249
0.005	0.0026	0.7746	0.0028	0.7601	0.0030	0.6405
Rise velocity						
0.040	0.0588		0.0632		0.0968	
0.020	0.0188	1.6421	0.0233	1.4365	0.0479	1.0148
0.010	0.0086	1.1298	0.0127	0.8800	0.0263	0.8649
0.005	0.0049	0.7979	0.0071	0.8386	0.0147	0.8397
Circularity						
0.040	0.0280		0.0329		0.0596	
0.020	0.0118	1.2469	0.0138	1.2566	0.0227	1.3932
0.010	0.0042	1.4797	0.0051	1.4403	0.0093	1.2879
0.005	0.0021	0.9860	0.0027	0.9238	0.0049	0.9290

Table VII. Model 2: Relative error norms and convergence orders for test case 1.

$\epsilon$	$\ e\ _1$	ROC <sub>1</sub>	$\ e\ _2$	ROC <sub>2</sub>	$\ e\ _\infty$	ROC <sub><math>\infty</math></sub>
Center of mass						
0.040	0.0117		0.0154		0.0302	
0.020	0.0021	2.4942	0.0025	2.6478	0.0047	2.7000
0.010	0.0013	0.6538	0.0017	0.5712	0.0030	0.6115
0.005	0.0015	-0.1534	0.0020	-0.2711	0.0036	-0.2228
Rise velocity						
0.040	0.0879		0.0977		0.1625	
0.020	0.0106	3.0468	0.0130	2.9105	0.0327	2.3125
0.010	0.0117	-0.1403	0.0134	-0.0411	0.0214	0.6113
0.005	0.0104	0.1791	0.0119	0.1649	0.0170	0.3354
Circularity						
0.040	0.0181		0.0209		0.0354	
0.020	0.0041	2.1593	0.0050	2.0667	0.0115	1.6236
0.010	0.0040	0.0061	0.0058	-0.2260	0.0122	-0.0898
0.005	0.0030	0.4082	0.0042	0.4697	0.0081	0.5850

Table VIII. Model 3: Relative error norms and convergence orders for test case 1.

$\epsilon$	$\ e\ _1$	ROC <sub>1</sub>	$\ e\ _2$	ROC <sub>2</sub>	$\ e\ _\infty$	ROC <sub><math>\infty</math></sub>
Center of mass						
0.040	0.0205		0.0218		0.0238	
0.020	0.0090	1.1801	0.0096	1.1901	0.0098	1.2764
0.010	0.0045	0.9920	0.0048	0.9962	0.0047	1.0623
0.005	0.0026	0.7835	0.0028	0.7695	0.0030	0.6484
Rise velocity						
0.040	0.0570		0.0617		0.0978	
0.020	0.0188	1.6024	0.0236	1.3860	0.0486	1.0072
0.010	0.0087	1.1134	0.0129	0.8724	0.0266	0.8731
0.005	0.0050	0.8020	0.0071	0.8504	0.0148	0.8392
Circularity						
0.040	0.0286		0.0336		0.0605	
0.020	0.0123	1.2192	0.0143	1.2282	0.0238	1.3463
0.010	0.0045	1.4422	0.0054	1.4163	0.0094	1.3451
0.005	0.0022	1.0083	0.0028	0.9516	0.0050	0.9170

Table IX. Relative error norms and convergence orders for test case 1 assuming the finest grid solution as exact solution.

$\epsilon$	Model 1		Model 2		Model 3	
	$\ e\ _1$	ROC <sub>1</sub>	$\ e\ _1$	ROC <sub>1</sub>	$\ e\ _1$	ROC <sub>1</sub>
Center of mass						
0.040	0.0167		0.0131		0.0172	
0.020	0.0060	1.4721	0.0032	2.0262	0.0057	1.5942
0.010	0.0019	1.6927	0.0005	2.8251	0.0016	1.8237
Rise velocity						
0.040	0.0559		0.0979		0.0551	
0.020	0.0157	1.8352	0.0172	2.5124	0.0174	1.6613
0.010	0.0041	1.9310	0.0030	2.5366	0.0046	1.9214
Circularity						
0.040	0.0259		0.0212		0.0255	
0.020	0.0097	1.4184	0.0030	2.8293	0.0102	1.3193
0.010	0.0021	2.1842	0.0014	1.0595	0.0025	2.0423

[1] in Figure 5. All three models seem to approach the reference solution for decreasing  $\epsilon$ . The differences between the models 1 and 3 are very small and vanish as  $\epsilon$  decreases. Model 2 deviates from the other two.

#### 5.4. Results for test case 2

In test case 2, the decrease in surface tension causes the bubble to develop a more non-convex shape and thin filaments, which eventually break off. This is a much harder problem, and also in [1], agreement between the used numerical approaches could not be achieved. It even remains unclear if break off really should occur for this setting. The results in [1] show that the size of the filaments might become very small (e.g., 0.01). Therefore, one can expect phase field methods to have some trouble because this can be close to the interface thickness  $\epsilon$ .

We again compare bubble shapes at final time for different values of  $\epsilon$  (Figure 6). At least for  $\epsilon = 0.04$ , there are visible differences between all of the three models. In opposite to the results

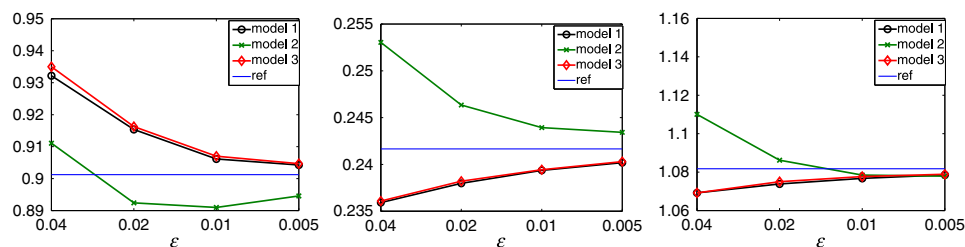
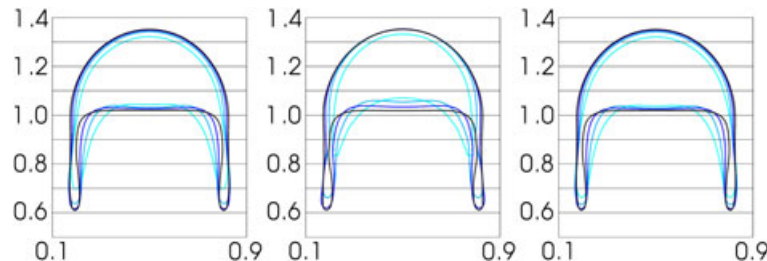


Figure 5. Minimum circularity, maximum rise velocity, and final center of mass (from left to right) for test case 1 and models 1–3 in comparison with the reference solution.

Figure 6. Bubble shapes for test case 2 at time  $t = 3$  for  $\epsilon = 0.04$  (light blue),  $\epsilon = 0.02$  (blue),  $\epsilon = 0.01$  (dark blue),  $\epsilon = 0.005$  (black) for models 1–3 (from left to right).

in [1], none of our models yields break off. Splitting did not even occur in tests with smaller  $\epsilon$  and higher grid resolution ( $\epsilon = 0.0005$ ,  $h_{\text{int}} = 1/1024$ ). However, one can see that in all models, the filaments become thinner for smaller  $\epsilon$ . Therefore, it is possible that break off happens for  $\epsilon \rightarrow 0$ .

Until the break off occurs in the reference solution, the bubble shapes agree well with the desired shapes for smaller  $\epsilon$ . The number of DOF and CPU time are comparable with test case 1 (Figure II).

To compare more quantitatively, we give the values of the benchmark quantities in Tables X–XII. Here, we restricted the comparison with the time interval  $[0, 2]$  because also the reference solutions do not agree well for later times.

Furthermore, we plot the circularity, center of mass, and rise velocity over time in Figures 7–9. All quantities seem to converge for each model. However, even for the finest grid ( $\epsilon = 0.005$ ), differences remain visible. We conclude that the resolution is still not fine enough to get sufficiently close to the reference solution. The plots for models 1 and 3 are almost indistinguishable, whereas model 2 reveals different time evolutions of all quantities.

Table X. Model 1: Minimum circularity and maximum rise velocity, with corresponding incidence times and final position of the center of mass for test case 2.

$\epsilon$	$c_{\min}$	$t _{c=c_{\min}}$	$V_{c,\max}$	$t _{V_c=V_{c,\max}}$	$y_c(t=3)$
0.040	0.6779	2.0000	0.2527	0.7360	0.8891
0.020	0.6669	2.0000	0.2520	0.7960	0.8998
0.010	0.6663	2.0000	0.2491	0.7100	0.9060
0.005	0.6718	2.0000	0.2491	0.7380	0.9099
ref	0.6901	2.0000	0.2502	0.7300	0.9154

Table XI. Model 2: Minimum circularity and maximum rise velocity, with corresponding incidence times and final position of the center of mass for test case 2.

$\epsilon$	$c_{\min}$	$t _{c=c_{\min}}$	$V_{c,\max}$	$t _{V_c=V_{c,\max}}$	$y_c(t=3)$
0.040	0.6817	1.9840	0.2483	0.8480	0.8932
0.020	0.6527	2.0000	0.2502	0.7320	0.9058
0.010	0.6614	2.0000	0.2500	0.6980	0.9115
0.005	0.6741	2.0000	0.2503	0.7180	0.9125
ref	0.6901	2.0000	0.2502	0.7300	0.9154

Table XII. Model 3: Minimum circularity and maximum rise velocity, with corresponding incidence times and final position of the center of mass for test case 2.

$\epsilon$	$c_{\min}$	$t _{c=c_{\min}}$	$V_{c,\max}$	$t _{V_c=V_{c,\max}}$	$y_c(t=3)$
0.040	0.6770	2.0000	0.2500	0.7680	0.8880
0.020	0.6684	1.9760	0.2503	0.7960	0.8994
0.010	0.6670	2.0000	0.2488	0.7100	0.9060
0.005	0.6722	2.0000	0.2490	0.7540	0.9098
ref	0.6901	2.0000	0.2502	0.7300	0.9154

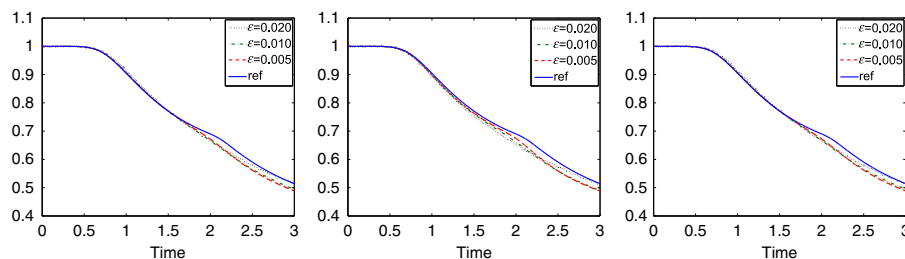


Figure 7. Circularity over time for test case 2 and models 1–3 (from left to right).

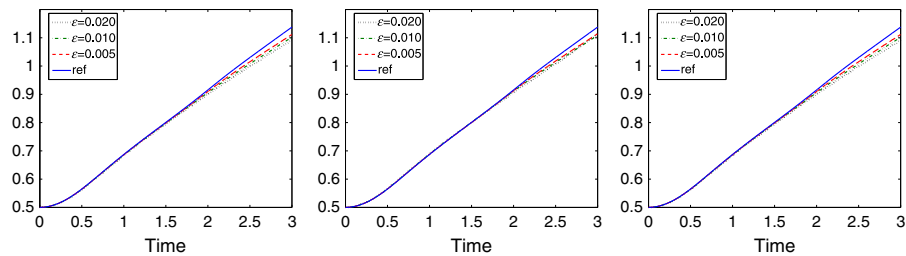


Figure 8. Center of mass over time for test case 2 and models 1–3 (from left to right).

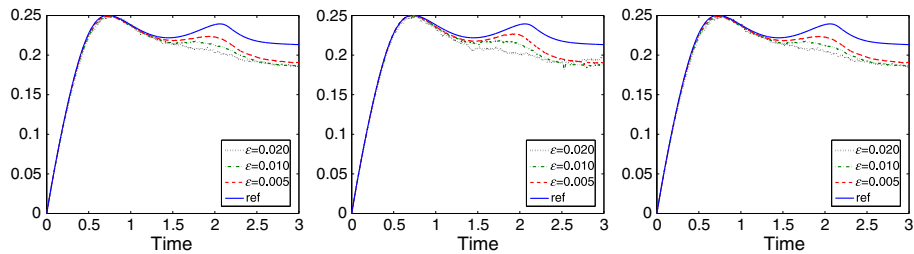


Figure 9. Rise velocity over time for test case 2 and models 1–3 (from left to right).

The relative error norms for the circularity, center of mass, and rise velocity are shown in Tables XIII–XV together with the estimated ROC. To calculate the errors, we use the reference solution from [1]. The ROC for the models 1 and 3 is in general less than one, clearly less than in test case 1. For model 2, we again obtain negative orders of convergence for the circularity for bigger  $\epsilon$ , which indicates that this model does not yet converge to the reference solution. However, the relative errors are comparable with those of the models 1 and 3.

Again, to make a fair comparison with the orders of convergence given in [1], we assume the solution on the finest grid to be the exact solution. Errors and orders of convergence are shown in Table XVI. We only display the  $\|\cdot\|_1$  norm, but the results are very similar in the other two norms. The observed ROC is more or less of order 1, which is significantly less than in test case 1.

Next, we plot the minimum circularity, maximum rise velocity, and final center of mass for all models versus the reference solution from [1] in Figure 10. Again, the differences between the models 1 and 3 are very small for the circularity and center of mass. However, for the maximum

Table XIII. Model 1: Relative error norms and convergence orders for test case 2.

$\epsilon$	$\ e\ _1$	ROC <sub>1</sub>	$\ e\ _2$	ROC <sub>2</sub>	$\ e\ _\infty$	ROC <sub>∞</sub>
Center of mass						
0.040	0.0121		0.0145		0.0288	
0.020	0.0061	0.9803	0.0079	0.8785	0.0170	0.7597
0.010	0.0031	0.9645	0.0043	0.8845	0.0102	0.7370
0.005	0.0020	0.6843	0.0026	0.7107	0.0061	0.7535
Rise velocity						
0.040	0.0555		0.0819		0.1922	
0.020	0.0364	0.6105	0.0529	0.6320	0.1376	0.4818
0.010	0.0252	0.5271	0.0366	0.5324	0.1049	0.3914
0.005	0.0146	0.7913	0.0214	0.7744	0.0623	0.7511
Circularity						
0.040	0.0151		0.0193		0.0374	
0.020	0.0065	1.2135	0.0087	1.1482	0.0241	0.6322
0.010	0.0040	0.6915	0.0069	0.3417	0.0240	0.0075
0.005	0.0024	0.7601	0.0046	0.5802	0.0183	0.3918

Table XIV. Model 2: Relative error norms and convergence orders for test case 2.

$\epsilon$	$\ e\ _1$	ROC <sub>1</sub>	$\ e\ _2$	ROC <sub>2</sub>	$\ e\ _\infty$	ROC <sub><math>\infty</math></sub>
Center of mass						
0.040	0.0050		0.0083		0.0242	
0.020	0.0028	0.8123	0.0038	1.1038	0.0105	1.2034
0.010	0.0014	1.0722	0.0017	1.2159	0.0042	1.3190
0.005	0.0009	0.6176	0.0012	0.4429	0.0031	0.4484
Rise velocity						
0.040	0.0661		0.0881		0.1886	
0.020	0.0449	0.5581	0.0618	0.5103	0.1512	0.3191
0.010	0.0236	0.9300	0.0347	0.8357	0.0987	0.6151
0.005	0.0132	0.8379	0.0182	0.9310	0.0526	0.9087
Circularity						
0.040	0.0057		0.0071		0.0164	
0.020	0.0121	-1.0891	0.0165	-1.2222	0.0374	-1.1886
0.010	0.0081	0.5745	0.0110	0.5851	0.0290	0.3641
0.005	0.0053	0.6070	0.0068	0.6870	0.0162	0.8407

Table XV. Model 3: Relative error norms and convergence orders for test case 2.

$\epsilon$	$\ e\ _1$	ROC <sub>1</sub>	$\ e\ _2$	ROC <sub>2</sub>	$\ e\ _\infty$	ROC <sub><math>\infty</math></sub>
Center of mass						
0.040	0.0130		0.0155		0.0299	
0.020	0.0064	1.0193	0.0082	0.9165	0.0175	0.7732
0.010	0.0033	0.9712	0.0044	0.8916	0.0106	0.7252
0.005	0.0020	0.7031	0.0027	0.7267	0.0061	0.7833
Rise velocity						
0.040	0.0584		0.0838		0.1920	
0.020	0.0374	0.6437	0.0534	0.6505	0.1395	0.4608
0.010	0.0259	0.5292	0.0369	0.5313	0.1055	0.4035
0.005	0.0150	0.7878	0.0216	0.7733	0.0627	0.7502
Circularity						
0.040	0.0151		0.0189		0.0352	
0.020	0.0063	1.2513	0.0085	1.1626	0.0247	0.5076
0.010	0.0039	0.6850	0.0066	0.3515	0.0232	0.0921
0.005	0.0023	0.7611	0.0045	0.5647	0.0179	0.3730

Table XVI. Relative error norms and convergence orders for test case 2 assuming the finest grid solution as exact solution.

$\epsilon$	Model 1		Model 2		Model 3	
	$\ e\ _1$	ROC <sub>1</sub>	$\ e\ _1$	ROC <sub>1</sub>	$\ e\ _1$	ROC <sub>1</sub>
Center of mass						
0.040	0.0102		0.0045		0.0110	
0.020	0.0042	1.2777	0.0022	1.0671	0.0044	1.3172
0.010	0.0012	1.8075	0.0010	1.1181	0.0013	1.7958
Rise velocity						
0.040	0.0446		0.0555		0.0464	
0.020	0.0234	0.9335	0.0327	0.7613	0.0237	0.9712
0.010	0.0109	1.1022	0.0112	1.5453	0.0111	1.0893
Circularity						
0.040	0.0151		0.0091		0.0151	
0.020	0.0042	1.8309	0.0069	0.3992	0.0041	1.8742
0.010	0.0017	1.3092	0.0029	1.2728	0.0017	1.2947

rise velocity, we observe quite high deviations, at least for bigger values of  $\epsilon$ . Although model 2 behaves different, it is closer to the reference solution than the other two models for all benchmark quantities. It is not clear if all three models really approach the reference solution for decreasing  $\epsilon$ .

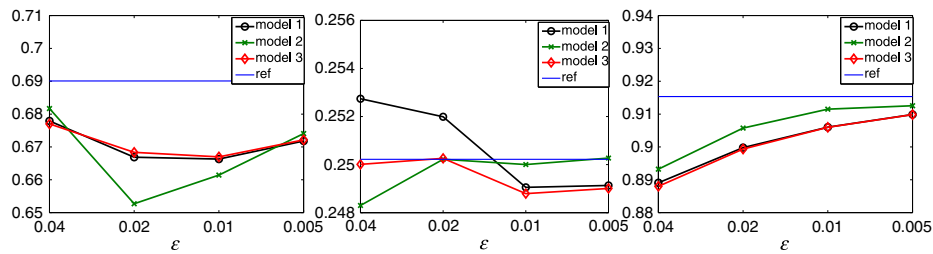


Figure 10. Minimum circularity, maximum rise velocity and final center of mass (from left to right) for test case 2 and models 1–3 in comparison to the reference solution.

## 6. SUMMARY

Diffuse interface models for two-phase flow have gained a lot of attention recently because they can easily handle moving contact lines and topological transitions without any need for reinitialization or convection stabilization. Various diffuse interface models have been proposed to deal with different densities and viscosities in both fluid phases. Three of them, namely the models of Boyer [5], Ding *et al.* [6], and Abels *et al.* [8], are compared in this work by applying them to the benchmark problem proposed in Hysing *et al.* [1]. This is to the best of our knowledge the first benchmark carried out for this type of models and the first comparison of these diffuse interface models among each other.

The benchmark is divided into two test cases, which both concern the evolution of a single bubble rising in a liquid column. We find that all the three models agree well with the results from [1] if the bubble undergoes only moderate shape deformations (test case 1). The time-averaged errors are higher, but the estimated order of convergence towards the finest grid solution is around 2 and therefore comparable with the results of Hysing *et al.* [1]. We see first order convergence towards the reference solution provided by [1]. The second test case is far more challenging, and it is not clear if the diffuse interface models converge to the same benchmark values as presented in [1]. Contrary to the results there, no break off occurred in our simulations. However, our calculations indicate first-order convergence towards the finest grid solution and lower order of convergence with respect to the reference solution. In both test cases, the differences between the calculated benchmark values of the two models of Ding *et al.* [6] and Abels *et al.* [8] are rather small and decrease as the interface thickness tends to zero. In summary, if combined with adaptive mesh refinement, diffuse interface methods are comparable in terms of accuracy and computational effort with level set approaches.

## ACKNOWLEDGEMENTS

SA and AV acknowledge the financial support from DFG Vo-899/6-2, SFB 609 TP C10, and DFG SPP-1506 (Vo-899/II-I).

## REFERENCES

1. Hysing S, Turek S, Kuzmin D, Parlani N, Burman E, Ganesan S, Tobiska L. Quantitative benchmark computations of two-dimensional bubble dynamics. *International Journal for Numerical Methods in Fluids* 2009; **60**:1259–1288.
2. Hohenberg PC, Halperin BI. Theory of dynamic critical phenomena. *Reviews of Modern Physics* 1977; **49**:435–479.
3. Gurtin ME, Poligone D, Vinale J. Two-phase fluids and immiscible fluids described by an order parameter. *Mathematical Models and Methods in Applied Sciences* 1996; **6**:815–831.
4. Lowengrub J, Trusinsowsky L. Quasi-incompressible Cahn–Hilliard fluids and topological transitions. *Proceedings of the Royal Society A* 1998; **454**:2617–2654.
5. Boyer F. A theoretical and numerical model for the study of incompressible mixture flows. *Computers & Fluids* 2002; **31**:41–68.
6. Ding H, Spelt PDM, Shu C. Diffuse interface model for incompressible two-phase flows with large density ratios. *Journal of Computational Physics* 2007; **226**:2078–2095.
7. Shen, Yang. A phase-field model and its numerical approximation for two-phase incompressible flows with different densities and viscosities. *SIAM Journal of Scientific Computing* 2010; **33**:1159–1179.

8. Abels H, Garcke H, Grün G. Thermodynamically consistent, frame invariant, diffuse interface models for incompressible two-phase flows with different densities. *preprint U Regensburg* 2011.
9. Anderson DM, McFadden GB, Wheeler AA. Diffuse interface methods in fluid mechanics. *Annual Review of Fluid Mechanics* 1998; **30**:139–165.
10. Emmerich H. Advances of and by phase-field modeling in condensed-matter physics. *Advances in Physics* 2008; **57**:1–87.
11. Singer-Loginova I, Singer H. The phase field technique for modeling multiphase materials. *Reports on Progress in Physics* 2008; **71**:106501.
12. Jaqmin D. Calculation of two-phase Navier–Stokes flows using phase-field modelling. *Journal of Computational Physics* 1999; **155**:96–127.
13. Feng X. Fully discrete finite element approximations of the Navier–Stokes–Cahn–Hilliard diffuse interface model for two-phase fluid flows. *SIAM Journal of Numerical Analysis* 2006; **44**:1049–1072.
14. Kay D, Welford R. Efficient numerical solution of Cahn–Hilliard–Navier–Stokes fluids in 2D. *SIAM Journal on Scientific Computing* 2007; **29**:2241–2257.
15. Aland S, Lowengrub J, Voigt A. Two-phase flow in complex geometries: a diffuse domain approach. *Computational Methods in Engineering Science* 2010; **1**:77–108.
16. Guermond JL, Quartapelle L. A projection fem for variable density incompressible flows. *Journal of Computational Physics* 2000; **165**:167–188.
17. Villanueva W, Amberg G. Some generic capillary-driven flows. *International Journal of Multiphase Flow* 2006; **32**:1072–1086.
18. Do-Quang M, Amberg G. The splash of a solid sphere impacting on a liquid surface: numerical simulation of the influence of wetting. *Physics of Fluids* 2009; **21**:022–102.
19. Teigen KE, Song P, Lowengrub J, Voigt A. A diffuse-interface method for two-phase flows with soluble surfactants. *Journal of Computational Physics* 2011; **230**:375–393.
20. Vey S, Voigt A. AMDiS: adaptive multidimensional simulations. *Computing and Visualization Science* 2007; **10**:57–67.
21. Davis TA. Algorithm 832: UMFPACK V4.3—an unsymmetric-pattern multifrontal method. *ACM Transactions on Mathematical Software* 2004; **30**:196–199.
22. Verfürth R. *A Review of a Posteriori Error Estimation and Adaptive Mesh-Refinement Techniques*. Wiley-Teubner Series Advances in Numerical Mathematics. John Wiley & Sons: Chichester, Stuttgart, 1996.
23. Feng X, Wu H.-J. A posteriori error estimates and an adaptive finite element method for the Allen–Cahn equation and the mean curvature flow. *Journal of Scientific Computing* 2005; **24**:121–146.